Article

Multiscale Investigation of the Structural, Electrical and Photoluminescence Properties of MoS$_2$ Obtained by MoO$_3$ Sulfurization

Salvatore E. Panasci [1,2], Antal Koos [3], Emanuela Schilirò [1], Salvatore Di Franco [1], Giuseppe Greco [1], Patrick Fiorenza [1], Fabrizio Roccaforte [1], Simonpietro Agnello [1,4,5], Marco Cannas [4], Franco M. Gelardi [4], Attila Sulyok [3], Miklos Nemeth [3], Béla Pécz [3,*] and Filippo Giannazzo [1,*]

1   Consiglio Nazionale delle Ricerche—Istituto per la Microelettronica e Microsistemi (CNR-IMM), Strada VIII 5, 95121 Catania, Italy; SalvatoreEthan.Panasci@imm.cnr.it (S.E.P.); Emanuela.Schiliro@imm.cnr.it (E.S.); salvatore.difranco@imm.cnr.it (S.D.F.); giuseppe.greco@imm.cnr.it (G.G.); Patrick.Fiorenza@imm.cnr.it (P.F.); fabrizio.roccaforte@imm.cnr.it (F.R.); simonpietro.agnello@unipa.it (S.A.)
2   Department of Physics and Astronomy, University of Catania, 95123 Catania, Italy
3   Centre for Energy Research, Institute of Technical Physics and Materials Science, Konkoly-Thege ut 29-33, 1121 Budapest, Hungary; koos.antal@ek-cer.hu (A.K.); sulyok.attila@ek-cer.hu (A.S.); nemeth.miklos@ek-cer.hu (M.N.)
4   Department of Physics and Chemistry Emilio Segrè, University of Palermo, 90123 Palermo, Italy; marco.cannas@unipa.it (M.C.); franco.gelardi@unipa.it (F.M.G.)
5   ATEN Center, University of Palermo, 90123 Palermo, Italy
*   Correspondence: pecz.bela@ek-cer.hu (B.P.); filippo.giannazzo@imm.cnr.it (F.G.)

Abstract: In this paper, we report a multiscale investigation of the compositional, morphological, structural, electrical, and optical emission properties of 2H-MoS$_2$ obtained by sulfurization at 800 °C of very thin MoO$_3$ films (with thickness ranging from ~2.8 nm to ~4.2 nm) on a SiO$_2$/Si substrate. XPS analyses confirmed that the sulfurization was very effective in the reduction of the oxide to MoS$_2$, with only a small percentage of residual MoO$_3$ present in the final film. High-resolution TEM/STEM analyses revealed the formation of few (i.e., 2–3 layers) of MoS$_2$ nearly aligned with the SiO$_2$ surface in the case of the thinnest (~2.8 nm) MoO$_3$ film, whereas multilayers of MoS$_2$ partially standing up with respect to the substrate were observed for the ~4.2 nm one. Such different configurations indicate the prevalence of different mechanisms (i.e., vapour-solid surface reaction or S diffusion within the film) as a function of the thickness. The uniform thickness distribution of the few-layer and multilayer MoS$_2$ was confirmed by Raman mapping. Furthermore, the correlative plot of the characteristic A$_{1g}$-E$_{2g}$ Raman modes revealed a compressive strain ($\varepsilon \approx -0.78 \pm 0.18\%$) and the coexistence of n- and p-type doped areas in the few-layer MoS$_2$ on SiO$_2$, where the p-type doping is probably due to the presence of residual MoO$_3$. Nanoscale resolution current mapping by C-AFM showed local inhomogeneities in the conductivity of the few-layer MoS$_2$, which are well correlated to the lateral changes in the strain detected by Raman. Finally, characteristic spectroscopic signatures of the defects/disorder in MoS$_2$ films produced by sulfurization were identified by a comparative analysis of Raman and photoluminescence (PL) spectra with CVD grown MoS$_2$ flakes.

Keywords: MoS$_2$; sulfurization; XPS; Raman; TEM; C-AFM; photoluminescence

1. Introduction

Transition metal dichalcogenides (TMDs) are a wide family of layered van der Waals (vdW) materials with the general chemical formula MX$_2$, M being a transition metal (Ti, Zr, Hf, V, Nb, Ta, Mo, W, Re, Pd, or Pt) and X a chalcogen atom (S, Se, or Te) [1]. Most of them exhibit metallic or semiconducting phases. In particular, semiconducting TMDs have been the object of increasing scientific interest in the last decade, due to their huge

potential for applications in several fields, including electronics, optoelectronics, spintronics, valleytronics, chemical/environmental sensing, energy generation, and catalysis [2–10]. Molybdenum disulfide (MoS_2) is the most investigated among TMDs, due to the natural abundance and good chemical/mechanical stability of its 2H semiconductor phase under ambient conditions. The bandgap tunability as a function of the thickness, with a transition from an indirect bandgap of ~1.2 eV for bulk or few-layer MoS_2 to a direct bandgap of ~1.8 eV for monolayer MoS_2 [11,12], makes this material appealing for optoelectronic and electronic applications. In fact, the first robust 2D transistor with a large on/off ratio and good field-effect mobility was demonstrated using monolayer $2H-MoS_2$ flakes as the semiconducting channel [13,14]. This material and other TMDs are currently considered a potential replacement of Si for the next generation of complementary metal oxide semiconductor (CMOS) devices allowing the continuation of Moore's law [15]. Furthermore, they can represent the basis for new concept (More-than-Moore) devices [16,17].

Due to this wide application potential, scalable and reproducible growth methods for thin films of TMDs are strongly required for their future implementation in manufacturing lines. In this context, research on MoS_2 wafer-scale growth and device integration is relatively more mature than for other 2D TMDs.

Top-down synthesis approaches used to separate MoS_2 from bulk crystals, such as mechanical exfoliation [18,19], gold-assisted exfoliation [20–24], and liquid exfoliation [25], are not suitable to ensure the reproducibility and thickness control on a wafer scale required for high-end electronic applications. For this reason, bottom-up approaches as Chemical Vapour Deposition (CVD) [26,27], Pulsed Laser Deposition (PLD) [28], Molecular Beam Epitaxy (MBE) [29], and Atomic Layer Deposition (ALD) [30] represent the most promising methods to obtain a reproducible thin film of TMDs on a large area.

In particular, CVD using vapours from S and MoO_3 powders has been widely explored by several research groups, since it is a cost-effective method to produce MoS_2 domains with good crystalline quality on different substrates [31–33]. Although monolayer flakes with a triangular or hexagonal shape and lateral extension from tens to hundreds of micrometres have been obtained under optimized CVD conditions [34], achieving coverage and thickness uniformity on the wafer scale still represents a huge challenge, due to the difficulty of controlling all the parameters involved in the process (including the substrate temperature, the evaporation rates of the S and Mo precursors, the pressure in the chamber, and the carrier gas flow rate) [35–39].

As an alternative to the single-step CVD approach, sulfurization of a Mo (or Mo-oxide) film pre-deposited on a substrate (e.g., by evaporation or sputtering) allows superior control of MoS_2 coverage and uniformity by controlling the initial film thickness [40–43]. Different to CVD (where the Mo–S bonds are mostly formed by vapour phase reaction and the MoS_2 lands on the substrate), the sulfurization process is a heterogeneous vapour-solid reaction between the S vapour and the pre-deposited film [44]. The conversion of MoO_x to MoS_2 by sulfurization has been demonstrated to occur in a wide temperature range, from 500 °C to 1000 °C, although the best quality films are typically obtained at temperatures > 750 °C [44]. Besides the vapour-solid surface reaction, the initial Mo or MoO_x film thickness also plays an important role in the process. In fact, with increasing its thickness, the diffusion of S in the film represents the limiting mechanism for the formation of MoS_2 layers and determines their alignment with respect to the substrate [45,46]. In particular, at typical sulfurization temperatures of 750–800 °C, single or few-layers of MoS_2 horizontally aligned to the substrate plane are obtained for very thin (<3 nm) Mo films, whereas vertically aligned growth occurs for thicker Mo films [47]. This is due to the favoured sulphur diffusion along the vdW gaps between the vertically oriented MoS_2 layers [45,47,48]. Besides the initial Mo (or Mo-oxide) thickness, other key factors controlling MoS_2 formation include the substrate heating rate, pressure, and local S concentration on the sample surface [49–51]. Furthermore, the underlying substrate can play an important role in MoS_2 formation during sulfurization of pre-deposited MoO_3. In fact, while a higher temperature may enhance the sulfurization degree, on the other hand, it can also result in increased MoO_3 evaporation

and diffusion of Mo atoms on the substrate surface. This latter phenomenon strongly depends on the adhesion energy and surface diffusivity of Mo atoms on the substrate.

The main disadvantage of the continuous MoS_2 films produced by the sulfurization approach is their nanocrystalline structure (with 20–30 nm grain-size) [44], typically resulting in poorer carrier mobility, if compared to the large and isolated monocrystalline MoS_2 flakes obtained by the CVD approach. However, the high uniformity and its good compatibility with the fabrication methods used in the semiconductor industry makes this approach appealing for some applications, e.g., MoS_2/semiconductor heterojunctions [52] or hydrogen evolution applications [53]. Hence, a detailed characterisation of structural/compositional, vibrational, optical, and electrical properties of MoS_2 films produced by Mo sulfurization remains highly desirable.

In this paper, few or multilayer MoS_2 on a SiO_2/Si substrate have been produced by sulfurization at 800 °C of very thin MoO_3 films, from ~2.8 nm to ~4.2 nm (i.e., the critical range for the transition from horizontally to vertically aligned layers). The compositional, morphological, structural, electrical, and optical emission properties of the grown films have been extensively investigated by the combination of several characterisation techniques with macro to nanoscale spatial resolution. This correlative analysis provides deep insight into the potentialities and limitations of this material system for applications.

2. Materials and Methods

The thin molybdenum-oxide films on SiO_2 (900 nm)/Si substrates were obtained by DC magnetron sputtering from a Mo-target (using a Quorum Q300-TD system), followed by natural oxidation in air. The sulfurization process, schematically illustrated in Figure 1, was carried out in a two-heating zones furnace (TSH12/38/500, Elite Thermal Systems Ltd., Market Harborough, UK), with the first zone (at a temperature of 150 °C) hosting a crucible with 300 mg sulphur (purity 99.9%, product 28260.234, VWR Chemicals, Radnor, PA, USA), and the second zone (at a temperature of 800 °C) hosting the MoO_3/SiO_2/Si sample. Starting from a base pressure of 4×10^{-6} bar, the Ar carrier gas (purity 5.0, Messer, Budapest, Hungary) with a flux of 100 sccm transported the S vapours from the first to the second zone. The duration of the sulfurization process was 60 min.
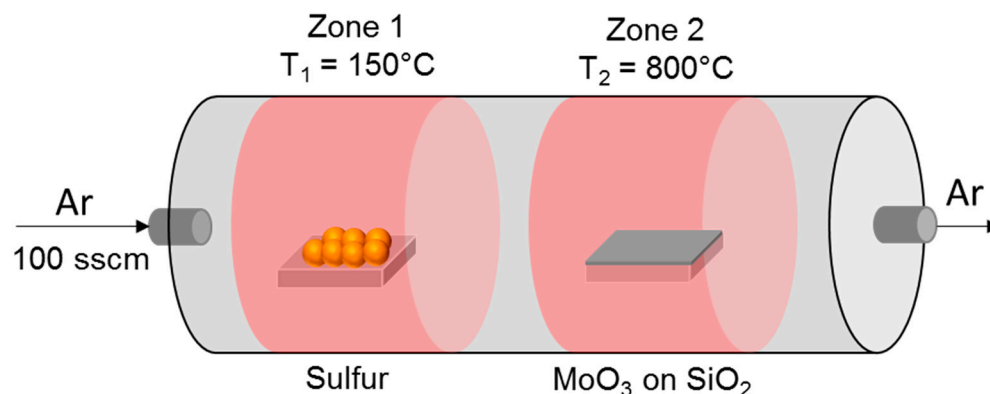

Figure 1. Schematic illustration of the sulfurization process of the thin MoO_3 films on the SiO_2/Si substrates.

Morphological analyses on the as-deposited MoO_3 films and after the sulfurization process were carried out by Tapping mode Atomic Force Microscopy using a DI3100 system by Bruker (Santa Barbara, CA, USA) with Nanoscope V electronics. The compositional properties of the as-deposited metal films and MoS_2 formation after the sulfurization process were evaluated by X-ray photoelectron spectroscopy (XPS) using Escalab Xi+ equipment by Thermo Fisher (Waltham, MA, USA), with a monochromatic Al Kα X-ray source (energy = 1486.6 eV). The spectra were collected at a take-off angle of 90° relative to the sample surface and pass energy of 20 eV. The instrument resolution was 0.45 eV (FWHM of the Ag $3d_{5/2}$ peak). The spectra were aligned using C1s (285 eV) as reference.

High-resolution transmission electron microscopy (HR-TEM), high angle annular dark-field scanning transmission electron microscopy (HAADF-STEM), and energy dispersion spectroscopy (EDS) analyses of the MoS_2 thin films were carried out with an aberration-corrected Titan Themis 200 microscope by Thermo Fisher (Waltham, MA USA). To this aim, cross-sectioned samples were prepared by a focused ion beam (FIB). Raman spectroscopy and mapping of MoS_2 vibrational peaks were carried out by WiTec Alpha equipment by WiTec (Ulm, Germany), using laser excitation at 532 nm, 1.5 mW power, and 100× objective. Photoluminescence spectra (PL) were collected using a Horiba (Palaiseau, France) system with a laser source of 532 nm. To confirm the uniformity of the MoS_2 thin layer across the substrate, the Raman and PL analyses have been performed at different positions on the sample. Finally, nanoscale resolution current mapping of MoS_2 on SiO_2 was performed by conductive Atomic Force Microscopy (C-AFM) with a DI3100 system by Bruker (Santa Barbara, CA, USA), using Pt-coated Si tips with ~5 nm curvature radius.
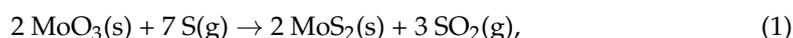
3. Results and Discussion

Figure 2a shows a typical AFM morphology of as-deposited MoO_3 on the SiO_2/Si substrate using the lowest sputtering time (30 s). This analysis indicates a very low root mean square (RMS) surface roughness of 0.35 nm. Similar roughness values have been measured for MoO_3 film thicknesses deposited at higher sputtering times. The thickness of the as-deposited films was also evaluated by AFM step height measurements performed on intentionally scratched regions of the films. Figure 2b,c show the morphologies and corresponding line profiles for films deposited with two different sputtering times (30 s and 45 s), resulting in ~2.8 nm and ~4.2 nm thickness, respectively.
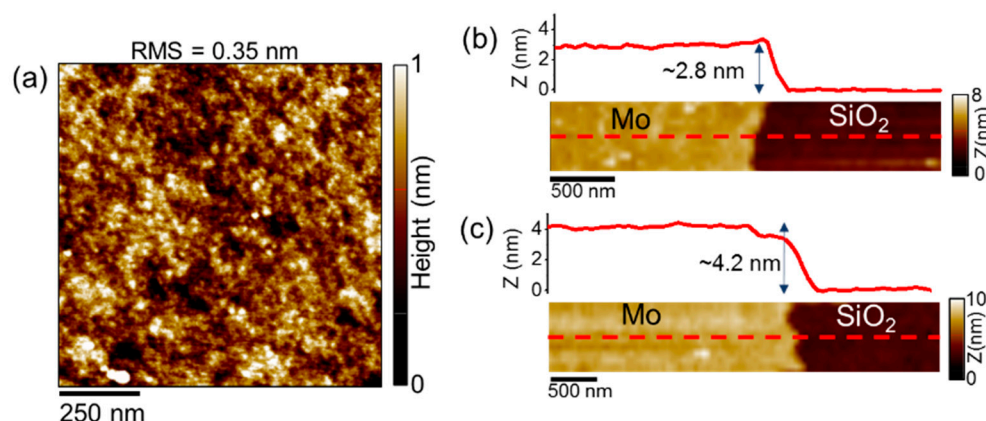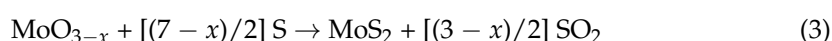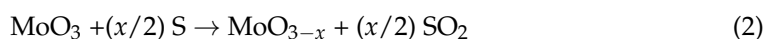

Figure 2. (**a**) Typical AFM morphology of as-deposited MoO_3 thin films on SiO_2, with the indication of the root mean square (RMS) roughness. (**b**,**c**) Determination of the thickness of films deposited with two different sputtering times by measurement of the step heights (~2.8 nm and ~4.2 nm) with respect to SiO_2 on scratched regions.

XPS compositional analyses performed on the thinnest deposited films revealed that they are predominantly composed of MoO_3, with a small (<1%) MoO_2 contribution. Recently, Vangelista et al. [44] also reported the complete oxidation (ascribed to air exposure after the deposition) of evaporated Mo films with similar thickness, used for subsequent MoS_2 growth by sulfurization. The same authors [44] explained the conversion of MoO_3 to MoS_2 upon exposure to sulphur according to the following chemical reaction:

$$2\,MoO_3(s) + 7\,S(g) \rightarrow 2\,MoS_2(s) + 3\,SO_2(g), \tag{1}$$

which is the result of two intermediate steps:

$$MoO_3 + (x/2)\,S \rightarrow MoO_{3-x} + (x/2)\,SO_2 \tag{2}$$

$$MoO_{3-x} + [(7-x)/2]\,S \rightarrow MoS_2 + [(3-x)/2]\,SO_2 \tag{3}$$

i.e., the S-induced reduction of the MoO_3 to a sub-stoichiometric oxide MoO_{3-x} (2), followed by its conversion to MoS_2 (3), with the formation of gaseous SO_2 as a by-product.

After the sulfurization process at 800 °C, XPS analyses were performed to evaluate the successful conversion of MoO_3 to MoS_2. Figure 3a reports an overview spectrum, allowing the quantification of the percentage of elemental concentrations on the sample surface. In particular, molybdenum and sulphur percentages of 3.26% and 6.82%, respectively, were evaluated (besides the large Si and O background), which were close to the stoichiometric [Mo]/[S] ratio for MoS_2. More detailed information on the Mo and S bonding was deduced from the $Mo3d_{3/2}$, $Mo3d_{5/2}$, and S2s core levels in Figure 3b, and the $S2p_{1/2}$ and $S2p_{3/2}$ core levels in Figure 3c. Two doublets were found in the Mo 3d spectrum, and both doublets were fitted with a peak separation of 3.1 eV [44,54,55]. In particular, the deconvolution of the Mo3d peaks shows the predominance of the Mo^{4+} component, associated with 2H-MoS_2, accompanied by a smaller Mo^{6+} contribution, associated with the presence of residual MoO_3. The two $S2p_{1/2}$ and $S2p_{3/2}$ peaks [44,54,55] in Figure 3c confirm that sulphur is mainly in the form of sulphide, with a small S-O component.
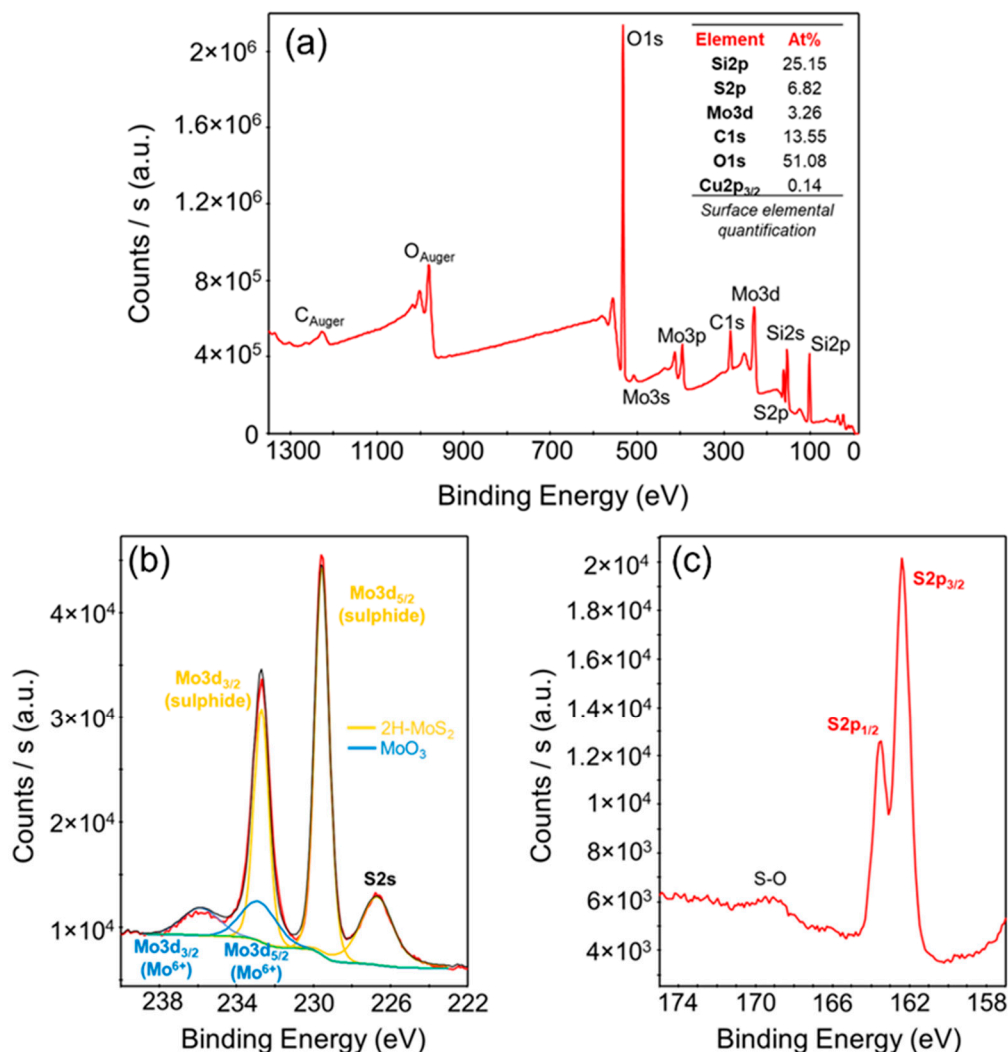
Figure 3. (**a**) Survey XPS spectrum of MoS_2 on SiO_2 produced by sulfurization of the 2.8 nm MoO_3 film, with the indication of the evaluated surface elemental composition. (**b**) XPS spectra of the Mo 3d and S 2s core levels, with the deconvolution of the Mo^{4+} contribution (related to MoS_2) and the Mo^{6+} contribution (related to residual MoO_3). (**c**) S 2p core levels spectra, indicating the predominance of the sulphide contribution, with a small S-O component.

The structural properties of the MoS_2 films were also investigated at nanoscale by transmission electron microscopy on cross-sectioned samples. Figure 4a,b show representative HR-TEM and HAADF-STEM analyses on the few-layers MoS_2 sample obtained by sulfurization of the ~2.8 nm MoO_3 film. The diffraction contrast in the HR-TEM image Figure 4a demonstrates the presence of two or three crystalline layers embedded between the amorphous SiO_2 substrate and amorphous carbon (a–c) protective film. These layers are predominantly oriented parallel to the substrate, with nanometric scale corrugations. Furthermore, an interlayer spacing of ~0.6 nm is directly evaluated from the HRTEM image of a 3L-MoS_2 reported in the insert of Figure 4a. The number of MoS_2 layers and their nearly parallel orientation with respect to the substrate is confirmed by the HAADF-STEM image in Figure 4b collected on the same sample. On the other hand, a more irregular configuration of the layers can be observed from the HRTEM (Figure 4c) and HAADF-STEM (Figure 4d) analyses performed on the MoS_2 multilayer produced by sulfurization of ~4.2 nm film. In fact, in the analysed specimen volume, horizontally oriented MoS_2 layers co-exist with layers standing up with respect to the SiO_2 surface. This observation is fully consistent with previous reports showing a transition from horizontal to vertically oriented growth for film thickness larger than 3 nm [47].
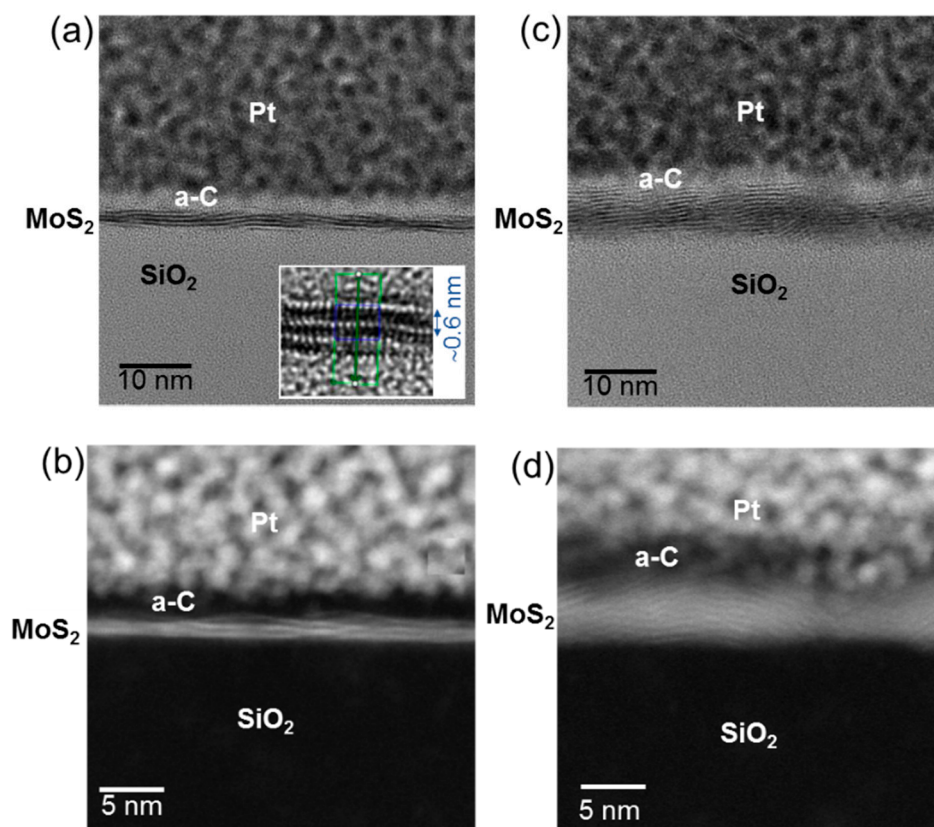
Figure 4. Cross sectional HR-TEM (**a**) and HAADF-STEM (**b**) images of few-layers MoS_2 obtained by sulfurization of the ~2.8 nm MoO_3 film on the SiO_2 substrate. MoS_2 is composed by nearly horizontally aligned 2–3 layers. The interlayer spacing in a 3-layers region is evaluated from the HR-TEM in the insert of panel (**a**). Cross sectional HR-TEM (**c**) and HAADF-STEM (**d**) of multilayers MoS_2 obtained by sulfurization of the ~4.2 nm MoO_3 film.

The layers number uniformity of the grown MoS_2 films was also investigated on micrometer scale areas and with high statistics by Raman spectroscopy. Figure 5 shows two typical Raman spectra of the few-layers (i.e., 2 L–3 L) MoS_2 (black line) and of the multilayer MoS_2 (red line) grown on SiO_2 by the sulfurization process. The two characteristic in-plane (E_{2g}) and out-of-plane (A_{1g}) vibrational modes of MoS_2 are clearly identified, and the typical redshift of the E_{2g} peak and blue shift of the A_{1g} with increasing the number

of layers [19] is observed. In particular, the difference $\Delta\omega = \omega_{A1g} - \omega_{E2g}$ between the wavenumbers of these two main modes is commonly taken as a way to evaluate the number of MoS_2 layers, with larger $\Delta\omega$ values generally associated with a thicker MoS_2.
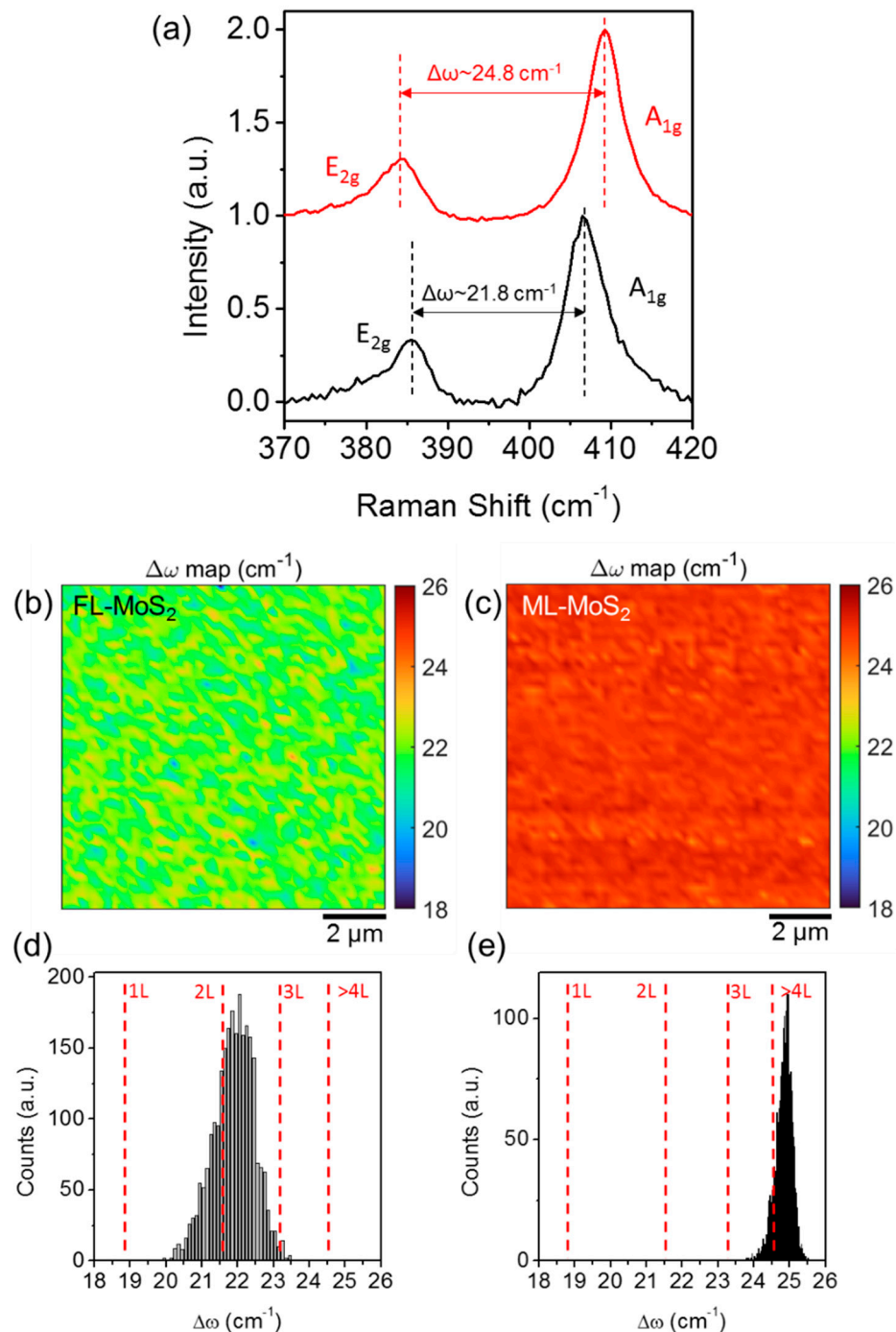
Figure 5. (**a**) Representative Raman spectra of the few-layers (FL) MoS_2 (black-line) and multilayer (ML) MoS_2 samples obtained by sulfurization of the 2.8 and 4.2 nm MoO_3 films on SiO_2. Colour maps of the A_{1g}-E_{2g} wavenumber difference $\Delta\omega$ obtained from arrays of Raman spectra collected on 10 μm $\times$ 10 μm scan areas on the FL-MoS_2 (**b**) and on the ML-MoS_2 (**c**) samples. Histogram of $\Delta\omega$ values showing a distribution with a peak at $\omega \approx 21.8 \pm 0.6$ cm^{-1} for the FL-MoS_2 sample associated to 2 L–3 L MoS_2 (**d**) and $\omega \approx 24.8 \pm 0.4$ cm^{-1} for the ML-MoS_2 sample, corresponding to >4 L MoS_2 thickness (**e**).

The colour maps in Figure 5b,c illustrate the spatial distribution of the $\Delta\omega$ values obtained from arrays of 50 × 50 Raman spectra collected on 10 µm × 10 µm scan areas. Figure 5d,e show the histograms of the $\Delta\omega$ values reported in the two maps, with the indication of the corresponding number of MoS$_2$ layers according to the calibration reported in Ref. [19]. The two distributions are quite uniform and exhibit a $\omega \approx 21.8 \pm 0.6$ cm^{-1} for the few-layer MoS$_2$ sample and $\omega \approx 24.8 \pm 0.4$ cm^{-1} for the multilayer MoS$_2$ sample. These $\Delta\omega$ values are associated with a 2 L–3 L MoS$_2$ thickness for the first sample, in very good agreement with TEM analyses in Figure 4, and to >4 L MoS$_2$ for the second one.

In the following, we will concentrate our attention on the 2 L–3 L MoS$_2$ sample, since the horizontal configuration of the layers makes it more suitable for electronic applications, similarly to 2H-MoS$_2$ samples produced by CVD or by exfoliation from bulk molybdenite.

The doping type and the biaxial strain (ε) of the thin MoS$_2$ film were also evaluated from the Raman maps by a correlative plot of A$_{1g}$ versus E$_{2g}$ peaks positions, as recently discussed in Ref. [23]. Figure 6a shows as blue circles the ω_{A1g} and ω_{E2g} values extracted from all the Raman spectra in the array of Figure 5. The red line in Figure 6a represents the ideal ω_{A1g} vs. ω_{E2g} dependence (i.e., the strain line) for a purely strained 3L-MoS$_2$ film. This relation is obtained from the combination of the following two expressions:

$$\omega_{E_{2g}} = \omega^0_{E_{2g}} - 2\gamma_{E_{2g}}\omega^0_{E_{2g}}\varepsilon \tag{4}$$

$$\omega_{A_{1g}} = \omega^0_{A_{1g}} - 2\gamma_{A_{1g}}\omega^0_{A_{1g}}\varepsilon \tag{5}$$

Here, $\gamma_{E_{2g}} = 0.39$ and $\gamma_{A_{1g}} = 0.09$ are the Grüneisen parameters for the two vibrational modes of 3L-MoS$_2$, estimated from the literature values of the peaks shift rates as a function of strain percentage (-3 cm^{-1}/% and -0.7 cm^{-1}/% for the E$_{2g}$ and A$_{1g}$ peaks, respectively) [56]. $\omega_{E^0_{2g}}$ and $\omega_{A^0_{1g}}$ represent the E$_{2g}$ and A$_{1g}$ frequencies for an ideally unstrained and undoped 3L-MoS$_2$. Here, the literature values for a suspended 3L-MoS$_2$ membrane ($\omega^0_{E_{2g}} = 382.9$ cm^{-1} and $\omega^0_{A_{1g}} = 406.4$ cm^{-1}) [56], not affected by the interaction with the substrate, were taken as the best approximation for these ideal values. This reference point is reported as a red square in Figure 6a, while the two arrows with opposite directions along the strain line indicate the tensile (red-shift) and compressive strain (blue-shift), respectively. Furthermore, the black dashed lines serve as guides to estimate the strain values. The distribution of the experimental points (blue circles) in the plot of Figure 6a clearly indicates that the thin MoS$_2$ film on SiO$_2$ is compressively strained. Figure 6b shows the 2D map of the compressive strain, calculated from the map of ω_{E2g} values by applying Equation (4). Furthermore, the corresponding histogram of the ε values is reported in Figure 6c, from which an average strain value $\varepsilon \approx -0.78\% \pm 0.18\%$ can be deduced.

The strain line separates the n-type and p-type doping regions in the $\omega_{A1g} - \omega_{E2g}$ diagram in Figure 6a. Noteworthy, the experimental points in Figure 6a are partially located in the n-type region and partially in the p-type one. Unintentional n-type doping is typically reported for MoS$_2$ films produced by different synthesis methods (such as mechanical exfoliation or CVD) and it is commonly ascribed to native defects present in the material [57–60]. Here, the observed p-type doping in some regions of the MoS$_2$ film produced by sulfurization can be associated with the presence of residual MoO$_3$, as deduced by XPS. In fact, several studies demonstrated how intentionally introducing MoO$_3$ in pristine (n-type) MoS$_2$, e.g., by O$_2$ plasma treatments, results in p-type doping of the material [61,62].
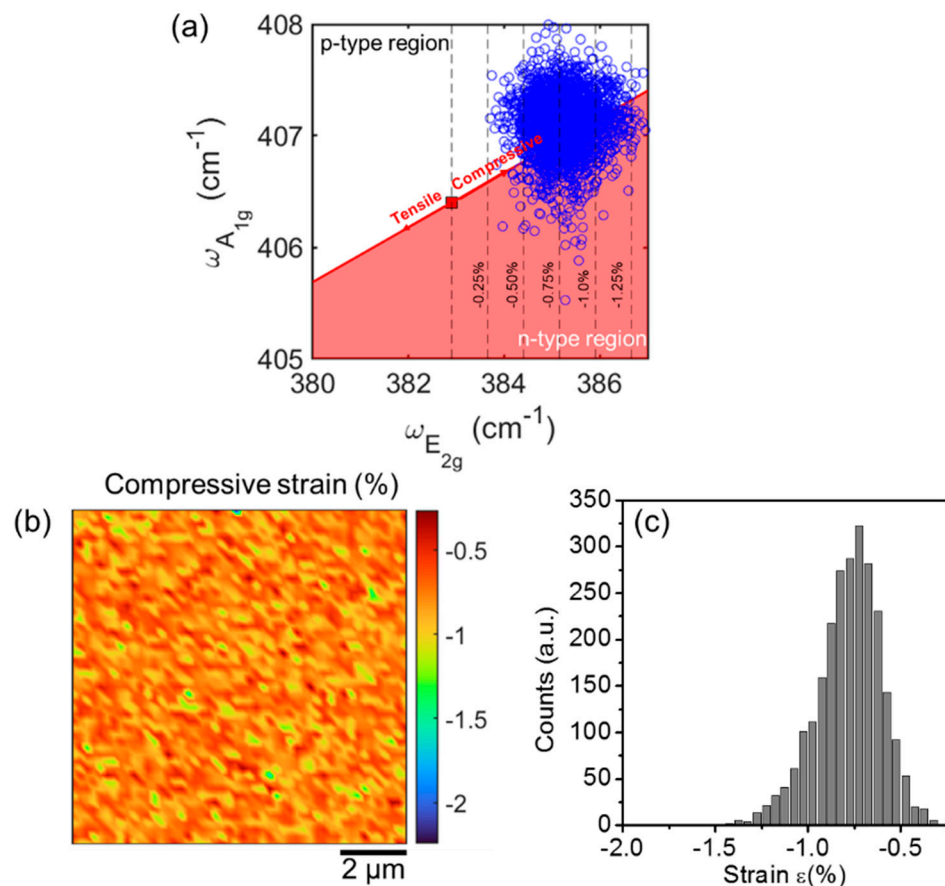
Figure 6. (**a**) Correlative plot of the ω_{A1g} and ω_{E2g} values (blue circles) extracted from all the Raman spectra in the array of Figure 5. The red line represents the ideal ω_{A1g} vs. ω_{E2g} dependence (i.e., the strain line) for a purely strained 3L-MoS$_2$ film. The red square corresponds to the frequencies $\omega_{E_{2g}^0}$ and $\omega_{A_{1g}^0}$ for an ideally unstrained and undoped 3L-MoS$_2$, while the two red arrows with opposite directions along the strain line indicate the tensile (red-shift) and compressive strain (blue-shift), respectively. (**b**) Map and (**c**) corresponding histogram of the compressive strain on a 10 μm × 10 μm area.

The MoS$_2$ thin layers produced by MoO$_3$ thin films sulfurization exhibit large resistivity values in the range of 10–100 Ω·cm [63]. This can be ascribed, in part, to the nanocrystalline structure of the films, i.e., the large density of grain boundaries, which are known to introduce resistive contributions in the current path [64]. On the other hand, the local changes in the compressive strain distribution, as well in the carrier density, deduced by Raman mapping is expected to have an effect on the electrical properties of the few-layers of MoS$_2$. To get direct information on the homogeneity of conductivity in this film, local current mapping has been carried out by C-AFM, as schematically depicted in Figure 7a. In this configuration, the current locally injected from the AFM metal tip flows in the MoS$_2$ film and is finally collected from the macroscopic front contact. Due to the nanoscale size of the tip contact, the dominant contributions to the measured resistance are represented by the local tip/MoS$_2$ contact resistance and the spreading resistance in the MoS$_2$ region underneath the tip. Figure 7b shows the contact-mode morphological image on the sample surface, from which an RMS roughness $\approx$ 0.5 nm slightly higher than the one of the as-deposited MoO$_3$ film (Figure 2a) was deduced. Figure 7c,d report the corresponding C-AFM current map and the histogram of the measured current values. The current map clearly shows submicrometer lateral variations of the conductivity, which are only partially correlated to the morphology, while the histogram shows a Gaussian distribution of these values, resembling the shape of the strain distribution in Figure 7d. From this comparison, we can speculate that these mesoscopic-scale inhomogeneities can

be partially ascribed to the lateral changes in the strain and carrier density detected by Raman.
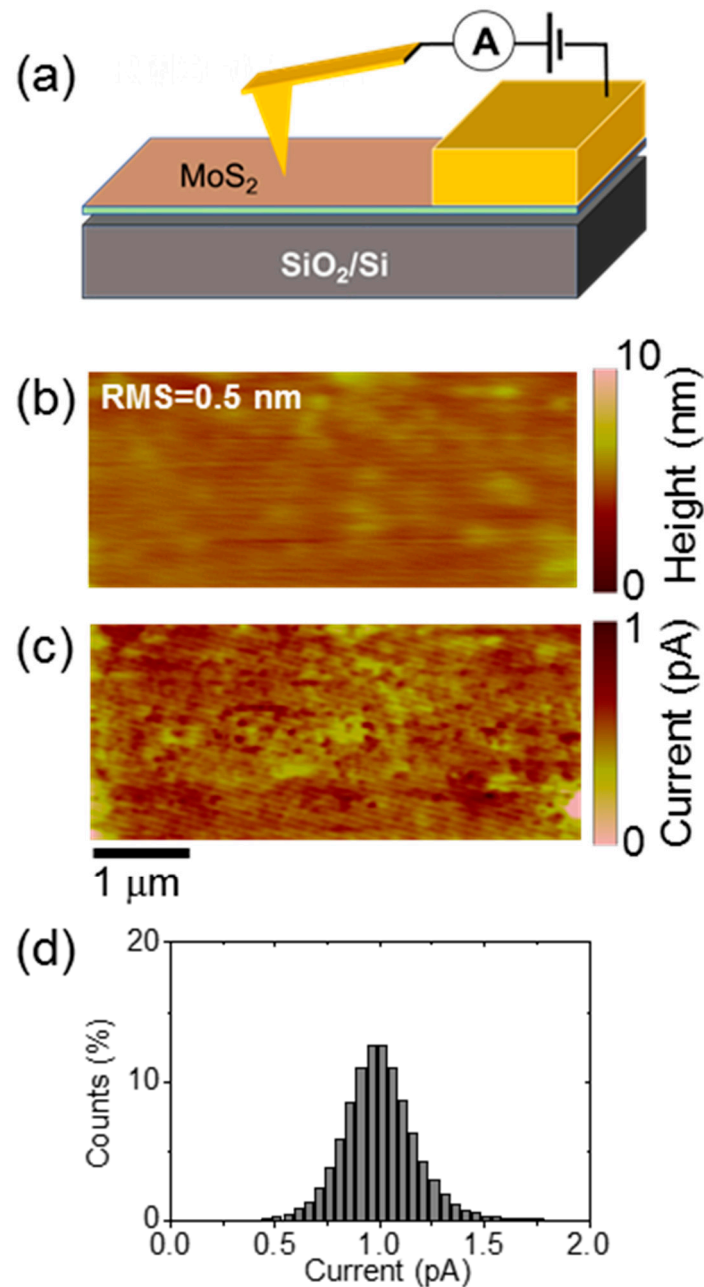

Figure 7. (**a**) Schematic of the C-AFM setup for local conductivity mapping of few-layers MoS_2 on SiO_2. (**b**) Morphology and (**c**) current map simultaneously measured with tip-to-sample bias of 5 V. (**d**) Histogram of current values from the C-AFM map.

In the last section of this paper, Raman and photoluminescence spectra acquired on the few-layers MoS_2 samples produced by sulfurization have been compared with reference spectra acquired on CVD-grown MoS_2 samples with a similar thickness.

Figure 8 shows a typical Raman spectrum of $3L$-MoS_2 on SiO_2 produced by MoO_3 sulfurization, compared with a spectrum of a $3L$-MoS_2 sample grown by CVD on SiO_2 [65], reported as reference. Some remarkable differences can be clearly observed between MoS_2 layers prepared using the two different approaches. In fact, besides a lower E_{2g}/A_{1g} intensity ratio, the two vibrational peaks exhibit a more pronounced asymmetric shape in the $3L$-MoS_2 produced by sulfurization as compared to the CVD-grown one. The
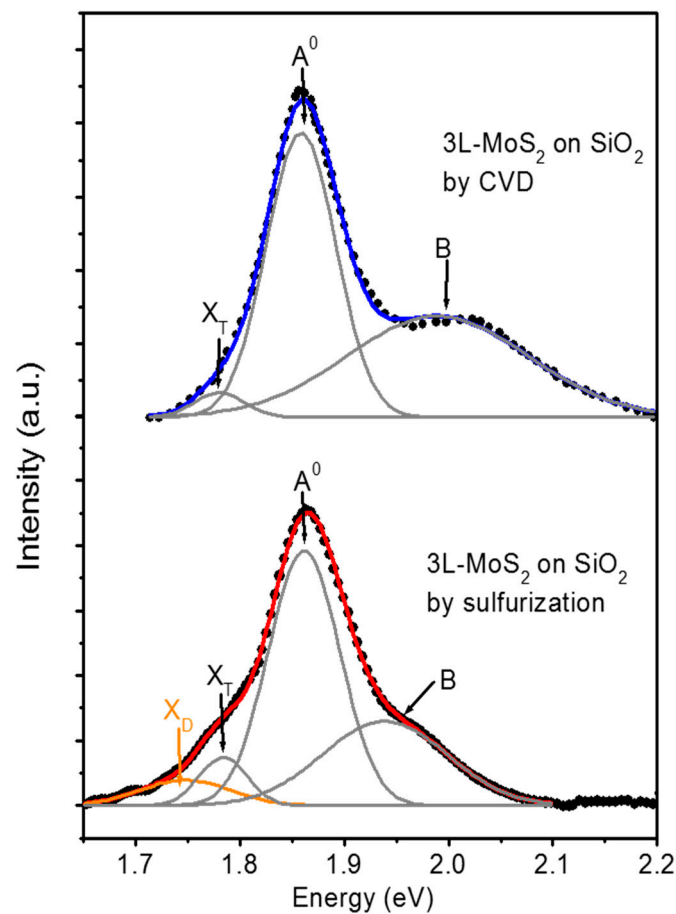
deconvolution analysis of the Raman spectra with four Gaussian contributions, associated with the main E_{2g} and A_{1g} modes and the disorder activated LO(M) and ZO(M) modes [66], is also presented in Figure 8. These LO(M) and ZO(M) components are very small in the Raman spectra of CVD 3L-MoS$_2$, whereas their weight is higher in the 3L-MoS$_2$ produced by sulfurization. In this latter case, they can be ascribed both to the nanocrystalline nature of the film, as well as to the presence of residual MoO$_3$, as deduced from the XPS analyses.
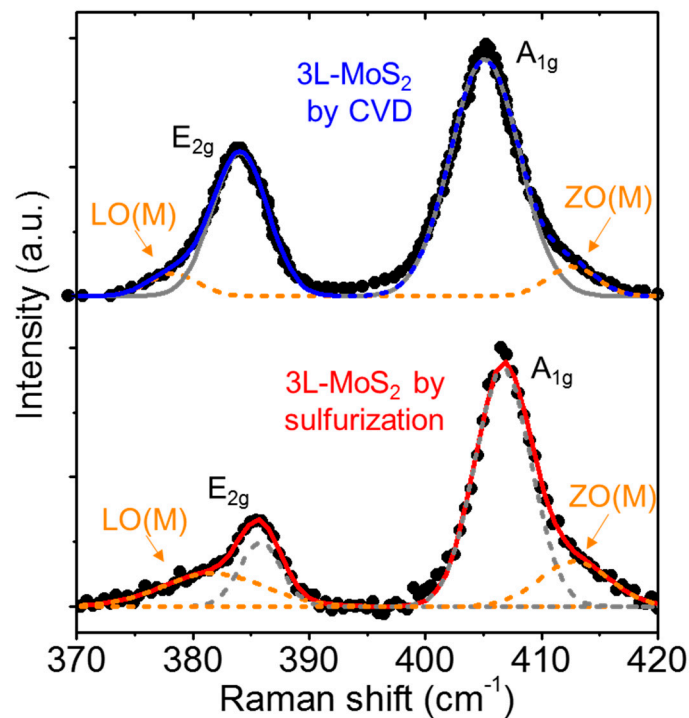
Figure 8. Raman spectrum for 3L-MoS$_2$ produced by sulfurization (red), compared with a reference spectrum for CVD grown 3L-MoS$_2$ (blue). Data for CVD 3L-MoS$_2$ were adapted with permission from [65], copyright Elsevier 2020.

Figure 9 shows the comparison between a PL spectrum measured on the 3L-MoS$_2$ produced by sulfurization with a reference spectrum for CVD grown 3L-MoS$_2$, taken from Ref. [65]. For both spectra, acquired using a 532 nm wavelength laser source, the main emission peak at an energy of 1.86 eV can be observed. However, significant differences in spectral features can be clearly identified from a detailed deconvolution analysis.

The PL spectrum of CVD MoS$_2$ can be fitted by three Gaussian peaks, associated with the two exciton contributions (A^0 at 1.86 $\pm$ 0.01 eV and B at 1.99 $\pm$ 0.01 eV, due to the spin-orbit splitting of the valence band) and the trionic contribution (X$_T$ at 1.78 $\pm$ 0.01 eV) [65]. On the other hand, the deconvolution analysis of the spectrum for the sulfurization grown sample allowed us to identify a fourth component X$_D$ at 1.75 $\pm$ 0.01 eV, besides the trion (X$_T$ at 1.78 $\pm$ 0.01 eV) and exciton peaks (A^0 at 1.86 $\pm$ 0.01 eV and B at 1.95 $\pm$ 0.01 eV). Noteworthy, the presence of this X$_D$ contribution is accompanied by a strong decrease in the spectral weight of the exciton peak B, as compared to the case of the CVD sample, as well as its FWHM reduction. The occurrence of a similar feature X$_D$, associated with point defects in the MoS$_2$ lattice, has been recently reported by Chow et al. [67] for the PL spectra of MoS$_2$ flakes subjected to soft Ar-plasma irradiation, and it was also accompanied by a decrease in the exciton peak B with respect to unirradiated flakes. Hence, the observed X$_D$ contribution for our samples produced by sulfurization was ascribed to a higher density of point defects with respect to CVD grown samples.

Figure 9. Photoluminescence (PL) spectra for 3L-MoS$_2$ produced by sulfurization, compared with a reference spectrum for CVD grown 3L-MoS$_2$. The deconvolution analysis indicated the presence of the excitonic contributions A^0, B, and of the trionic contribution X$_T$ (grey lines) for the CVD grown sample. In addition, the defect-related peak X$_D$ (orange line) is identified in the sulfurization grown sample. Data for CVD 3L-MoS$_2$ were adapted with permission from [65], copyright Elsevier 2020.

4. Conclusions

In conclusion, we reported a detailed analysis of the compositional, morphological, structural, electrical, and optical emission properties of few or multilayer MoS$_2$ on a SiO$_2$/Si substrate produced by sulfurization of very thin MoO$_3$ films at 800 °C. Both Raman mapping and TEM/STEM analyses showed the formation of 2–3 layers of MoS$_2$ nearly aligned with the SiO$_2$ surface after sulfurization of the thinnest MoO$_3$ film, whereas multilayers of MoS$_2$ (partially standing up) were observed for the thicker MoO$_3$ film. The strain distribution in the few-layer MoS$_2$ on SiO$_2$ was evaluated by the correlative plot of the characteristic A$_{1g}$-E$_{2g}$ Raman modes, showing the occurrence of a compressive strain $\varepsilon \approx -0.78 \pm 0.18\%$. Furthermore, the co-existence of submicrometer areas with n- and p-type doping is detected, with the p-type doping probably due to the presence of residual MoO$_3$, as revealed by XPS analyses. Nanoscale resolution current mapping by C-AFM showed conductivity inhomogeneities in the few-layer MoS$_2$, which are well correlated to the lateral changes in the strain detected by Raman. Finally, the characteristics spectroscopic signatures of the defects/disorder were identified by comparing Raman and PL spectra of sulfurization grown MoS$_2$ with reference analyses of CVD-grown single crystalline MoS$_2$.

The demonstrated MoS$_2$ growth method is quite versatile and can be extended to different substrates, besides SiO$_2$. In particular, the adoption of crystalline substrates (such as sapphire, GaN, and 4H-SiC) with the hexagonal basal plane and good lattice matching with MoS$_2$ is expected to enhance the domain size and electronic quality of the grown films. Furthermore, the homogeneous large area few-layer MoS$_2$ can be transferred to

arbitrary substrates (including flexible ones) [68] and find applications in different fields of microelectronics, flexible electronics, and sensing.

References

1. Manzeli, S.; Ovchinnikov, D.; Pasquier, D.; Yazyev, O.V.; Kis, A. 2D transition metal dichalcogenides. *Nat. Rev. Mater.* **2017**, *2*, 17033. [CrossRef]
2. Lopez-Sanchez, O.; Lembke, D.; Kayci, M.; Radenovic, A.; Kis, A. Ultrasensitive Photodetectors Based on Monolayer MoS_2. *Nat. Nanotechnol.* **2013**, *8*, 497–501. [CrossRef]
3. Yin, Z.; Li, H.; Li, H.; Jiang, L.; Shi, Y.; Sun, Y.; Lu, G.; Zhang, Q.; Chen, X.; Zhang, H. Single-Layer MoS_2 Phototransistors. *ACS Nano* **2012**, *6*, 74–80. [CrossRef] [PubMed]
4. Li, H.; Yin, Z.; He, Q.; Li, H.; Huang, X.; Lu, G.; Fam, D.W.H.; Tok, A.l.Y.; Zhang, Q.; Zhang, H. Fabrication of Single-and Multilayer MoS_2 Film-Based Field-Effect Transistors for Sensing NO at Room Temperature. *Small* **2012**, *8*, 63–67. [CrossRef] [PubMed]
5. Radisavljevic, B.; Whitwick, M.B.; Kis, A. Integrated Circuits and Logic Operations Based on Single-Layer MoS_2. *ACS Nano* **2011**, *5*, 9934–9938. [CrossRef] [PubMed]
6. Ayari, A.; Cobas, E.; Ogundadegbe, O.; Fuhrer, M.S. Realization and Electrical Characterization of Ultrathin Crystals of Layered Transition-Metal Dichalcogenides. *J. Appl. Phys.* **2007**, *101*, 014507. [CrossRef]
7. Luo, Y.K.; Xu, J.; Zhu, T.; Wu, G.; McCormick, E.J.; Zhan, W.; Neupane, M.R.; Kawakami, R.K. Opto-Valleytronic Spin Injection in Monolayer MoS_2/Few-Layer Graphene Hybrid Spin Valves. *Nano Lett.* **2017**, *17*, 3877–3883. [CrossRef]
8. Jiang, J.; Chen, Z.; Hu, Y.; Xiang, Y.; Zhang, L.; Wang, Y.; Wang, G.-C.; Shi, J. Flexo-photovoltaic effect in MoS_2. *Nat. Nanotechnol.* **2021**, *16*, 894–901. [CrossRef]
9. Hu, J.; Yu, L.; Deng, J.; Wang, Y.; Cheng, K.; Ma, C.; Zhang, Q.; Wen, W.; Yu, S.; Pan, Y.; et al. Sulfur vacancy-rich MoS_2 as a catalyst for the hydrogenation of CO_2 to methanol. *Nat. Catal.* **2021**, *4*, 242–250. [CrossRef]
10. Li, G.; Chen, Z.; Li, Y.; Zhang, D.; Yang, W.; Liu, Y.; Cao, L. Engineering Substrate Interaction To Improve Hydrogen Evolution Catalysis of Monolayer MoS_2 Films beyond Pt. *ACS Nano* **2020**, *14*, 1707–1714. [CrossRef]
11. Mak, K.F.; Lee, C.; Hone, J.; Shan, J.; Heinz, T.F. Atomically Thin MoS_2: A New Direct-Gap Semiconductor. *Phys. Rev. Lett.* **2010**, *105*, 136805. [CrossRef] [PubMed]
12. Kuc, A.; Zibouche, N.; Heine, T. Influence of Quantum Confinement on the Electronic Structure of the Transition Metal Sulfide TS_2. *Phys. Rev. B Condens. Matter Mater. Phys.* **2011**, *83*, 245213. [CrossRef]
13. Radisavljevic, B.; Radenovic, A.; Brivio, J.; Giacometti, V.; Kis, A. Single-Layer MoS_2 Transistors. *Nat. Nanotechnol.* **2011**, *6*, 147–150. [CrossRef] [PubMed]
14. Wu, W.; De, D.; Chang, S.C.; Wang, Y.; Peng, H.; Bao, J.; Pei, S.S. High mobility and high on/off ratio field-effect transistors based on chemical vapor deposited single-crystal MoS_2 grains. *Appl. Phys. Lett.* **2013**, *102*, 142106. [CrossRef]
15. Yoon, Y.; Ganapathi, K.; Salahuddin, S. How Good Can Monolayer MoS_2 Transistors Be? *Nano Lett.* **2011**, *11*, 3768–3773. [CrossRef] [PubMed]

16. Giannazzo, F.; Greco, G.; Roccaforte, F.; Sonde, S.S. Vertical Transistors Based on 2D Materials: Status and Prospects. *Crystals* **2018**, *8*, 70. [CrossRef]

17. Giannazzo, F. Engineering 2D heterojunctions with dielectrics. *Nat. Electron.* **2019**, *2*, 54. [CrossRef]

18. Novoselov, K.S.; Jiang, D.; Schedin, F.; Booth, T.J.; Khotkevich, V.V.; Morozov, S.V.; Geim, A.K. Two-dimensional atomic crystals. *Proc. Natl. Acad. Sci. USA* **2005**, *102*, 10451–10453. [CrossRef]

19. Lee, C.; Yan, H.; Brus, L.E.; Heinz, T.F.; Hone, J.; Ryu, S. Anomalous lattice vibrations of single-and few-layer MoS$_2$. *ACS Nano* **2010**, *4*, 2695–2700. [CrossRef]

20. Velický, M.; Donnelly, G.E.; Hendren, W.R.; McFarland, S.; Scullion, D.; DeBenedetti, W.J.I.; Correa, G.C.; Han, Y.; Wain, A.J.; Hines, M.A.; et al. Mechanism of Gold-Assisted Exfoliation of Centimeter-Sized Transition-Metal Dichalcogenide Monolayers. *ACS Nano* **2018**, *12*, 10463–10472. [CrossRef]

21. Desai, S.B.; Madhvapathy, S.R.; Amani, M.; Kiriya, D.; Hettick, M.; Tosun, M.; Zhou, Y.; Dubey, M.; Ager, J.W., III; Chrzan, D.; et al. Gold-Mediated Exfoliation of Ultralarge Optoelectronically-Perfect Monolayers. *Adv. Mater.* **2016**, *28*, 4053–4058. [CrossRef]

22. Magda, G.Z.; Pető, J.; Dobrik, G.; Hwang, C.; Biró, L.P.; Tapasztó, L. Exfoliation of Large-Area Transition Metal Chalcogenide Single Layers. *Sci. Rep.* **2015**, *5*, 14714. [CrossRef]

23. Panasci, S.E.; Schilirò, E.; Migliore, F.; Cannas, M.; Gelardi, F.M.; Roccaforte, F.; Giannazzo, F.; Agnello, S. Substrate impact on the thickness dependence of vibrational and optical properties of large area MoS$_2$ produced by gold-assisted exfoliation. *Appl. Phys. Lett.* **2021**, *119*, 093103. [CrossRef]

24. Panasci, S.E.; Schilirò, E.; Greco, G.; Cannas, M.; Gelardi, F.M.; Agnello, S.; Roccaforte, F.; Giannazzo, F. Strain, Doping, and Electronic Transport of Large Area Monolayer MoS$_2$ Exfoliated on Gold and Transferred to an Insulating Substrate. *ACS Appl. Mat. Interf.* **2021**, *13*, 31248–31259. [CrossRef] [PubMed]

25. Coleman, J.N.; Lotya, M.; O'Neill, A.; Bergin, S.D.; King, P.J.; Khan, U.; Young, K.; Gaucher, A.; De, S.; Smith, R.J.; et al. Two-dimensional nanosheets produced by liquid exfoliation of layered materials. *Science* **2011**, *331*, 568–571. [CrossRef] [PubMed]

26. Lee, Y.H.; Zhang, X.-Q.; Zhang, W.; Chang, M.-T.; Lin, C.-T.; Chang, K.-D.; Yu, Y.-C.; Wang, J.T.-W.; Chang, C.-S.; Li, L.-J.; et al. Synthesis of Large-Area MoS$_2$ Atomic Layers with Chemical Vapor Deposition. *Adv. Mater.* **2012**, *24*, 2320–2325. [CrossRef]

27. Zhan, Y.; Liu, Z.; Najmaei, S.; Ajayan, P.M.; Lou, J. Large-Area Vapor-Phase Growth and Characterization of MoS$_2$ Atomic Layers on a SiO$_2$ Substrate. *Small* **2012**, *8*, 966–971. [CrossRef]

28. Ho, Y.-T.; Ma, C.-H.; Luong, T.-T.; Wei, L.-L.; Yen, T.-C.; Hsu, W.-T.; Chang, W.-H.; Chu, Y.-C.; Tu, Y.-Y.; Pande, K.P.; et al. Layered MoS$_2$ Grown on c-Sapphire by Pulsed Laser Deposition. *Phys. Status Solidi RRL* **2015**, *9*, 187–191. [CrossRef]

29. Fu, D.; Zhao, X.; Zhang, Y.-Y.; Li, L.; Xu, H.; Jang, A.-R.; Yoon, S.I.; Song, P.; Poh, S.M.; Ren, T.; et al. Molecular Beam Epitaxy of Highly Crystalline Monolayer Molybdenum Disulfide on Hexagonal Boron Nitride. *J. Am. Chem. Soc.* **2017**, *139*, 9392–9400. [CrossRef]

30. Valdivia, A.; Tweet, D.J.; Conley, J.F., Jr. Atomic layer deposition of two dimensional MoS$_2$ on 150 mm substrates. *J. Vac. Sci. Technol.* **2016**, *34*, 21515. [CrossRef]

31. Najmaei, S.; Liu, Z.; Zhou, W.; Zou, X.; Shi, G.; Lei, S.; Yakobson, B.I.; Idrobo, J.-C.; Ajayan, P.M.; Lou, J. Vapour phase growth and grain boundary structure of molybdenum disulphide atomic layers. *Nat. Mater.* **2013**, *12*, 754–759. [CrossRef] [PubMed]

32. Liu, H.F.; Wong, S.L.; Chi, D.Z. CVD growth of MoS$_2$-based two-dimensional materials. *Chem. Vap. Depos.* **2015**, *21*, 241–259. [CrossRef]

33. Jeon, J.; Jang, S.K.; Jeon, S.M.; Yoo, G.; Jang, Y.H.; Park, J.H.; Lee, S. Layer-controlled CVD growth of large-area two-dimensional MoS$_2$ films. *Nanoscale* **2015**, *7*, 1688–1695. [CrossRef] [PubMed]

34. Chen, J.; Tang, W.; Tian, B.; Liu, B.; Zhao, X.; Liu, Y.; Ren, T.; Liu, W.; Geng, D.; Jeong, H.Y.; et al. Chemical Vapor Deposition of High-Quality Large-Sized MoS$_2$ Crystals on Silicon Dioxide Substrates. *Adv. Sci.* **2016**, *3*, 1600033. [CrossRef] [PubMed]

35. Zhang, Z.; Chen, P.; Duan, X.; Zang, K.; Luo, J.; Duan, X. Robust epitaxial growth of two-dimensional heterostructures, multiheterostructures, and superlattices. *Science* **2017**, *357*, 788–792. [CrossRef]

36. Liu, B.; Fathi, M.; Chen, L.; Abbas, A.; Ma, Y.; Zhou, C. Chemical vapor deposition growth of monolayer WSe$_2$ with tunable device characteristics and growth mechanism study. *ACS Nano* **2015**, *9*, 6119–6127. [CrossRef]

37. Tang, L.; Tan, J.; Nong, H.; Liu, B.; Cheng, H.M. Chemical Vapor Deposition Growth of Two-Dimensional Compound Materials: Controllability, Material Quality, and Growth Mechanism. *Acc. Mater. Res.* **2020**, *2*, 36–47. [CrossRef]

38. Wang, S.; Rong, Y.; Fan, Y.; Pacios, M.; Bhaskaran, H.; He, K.; Warner, J.H. Shape evolution of monolayer MoS$_2$ crystals grown by chemical vapor deposition. *Chem. Mater.* **2014**, *26*, 6371–6379. [CrossRef]

39. Yang, S.Y.; Shim, G.W.; Seo, S.B.; Choi, S.Y. Effective shape-controlled growth of monolayer MoS$_2$ flakes by powder-based chemical vapor deposition. *Nano Res.* **2017**, *10*, 255–262. [CrossRef]

40. Wu, C.R.; Chang, X.R.; Wu, C.H.; Lin, S.Y. The growth mechanism of transition metal dichalcogenides by using sulfurization of pre-deposited transition metals and the 2D crystal hetero-structure establishment. *Sci. Rep.* **2017**, *7*, 42146. [CrossRef]

41. Li, D.; Xiao, Z.; Mu, S.; Wang, F.; Liu, Y.; Song, J.; Huang, X.; Jiang, L.; Xiao, J.; Liu, L.; et al. A facile space-confined solid-phase sulfurization strategy for growth of high-quality ultrathin molybdenum disulfide single crystals. *Nano Lett.* **2018**, *18*, 2021–2032. [CrossRef] [PubMed]

42. Taheri, P.; Wang, J.; Xing, H.; Destino, J.F.; Arik, M.M.; Zhao, C.; Kang, K.; Blizzard, B.; Zhang, L.; Zhao, P. Growth mechanism of largescale MoS$_2$ monolayer by sulfurization of MoO$_3$ film. *Mater. Res. Expr.* **2016**, *3*, 075009. [CrossRef]

43. Hutar, P.; Spankova, M.; Sojkova, M.; Dobrocka, E.; Vegso, K.; Hagara, J.; Halahovets, Y.; Majkova, E.; Siffalovic, P.; Hulman, M. Highly crystalline MoS$_2$ thin films fabricated by sulfurization. *Phys. Status Solidi (B)* **2019**, *256*, 1900342. [CrossRef]

44. Vangelista, S.; Cinquanta, E.; Martella, C.; Alia, M.; Longo, M.; Lamperti, A.; Mantovan, R.; Basso Basset, F.; Pezzoli, F.; Molle, A. Towards a uniform and large-scale deposition of MoS$_2$ nanosheets via sulfurization of ultra-thin Mo based solid films. *Nanotechnology* **2016**, *27*, 175703. [CrossRef]

45. Kong, D.; Wang, H.; Cha, J.J.; Pasta, M.; Koski, K.J.; Yao, J.; Cui, Y. Synthesis of MoS$_2$ and MoSe$_2$ Films with Vertically Aligned Layers. *Nano Lett.* **2013**, *13*, 1341–1347. [CrossRef] [PubMed]

46. Cho, S.-Y.; Kim, S.J.; Lee, Y.; Kim, J.-S.; Jung, W.-B.; Yoo, H.-W.; Kim, J.; Jung, H.-T. Highly Enhanced Gas Adsorption Properties in Vertically Aligned MoS$_2$ Layers. *ACS Nano* **2015**, *9*, 9314–9321. [CrossRef]

47. Jung, Y.; Shen, J.; Liu, Y.; Woods, J.M.; Sun, Y.; Cha, J.J. Metal Seed Layer Thickness-Induced Transition from Vertical to Horizontal Growth of MoS$_2$ and WS$_2$. *Nano Lett.* **2014**, *14*, 6842–6849. [CrossRef]

48. Stern, C.; Grinvald, S.; Kirshner, M.; Sinai, O.; Oksman, M.; Alon, H.; Meiron, O.E.; Bar-Sadan, M.; Houben, L.; Naveh, D. Growth Mechanisms and Electronic Properties of Vertically Aligned MoS$_2$. *Sci. Rep.* **2018**, *8*, 16480. [CrossRef]

49. Shang, S.-L.; Lindwall, G.; Wang, Y.; Redwing, J.M.; Anderson, T.; Liu, Z.-K. Lateral Versus Vertical Growth of Two-Dimensional Layered Transition-Metal Dichalcogenides: Thermodynamic Insight into MoS$_2$. *Nano Lett.* **2016**, *16*, 5742–5750. [CrossRef]

50. Sojková, M.; Vegso, K.; Mrkyvkova, N.; Hagara, J.; Hutár, P.; Rosová, A.; Čaplovičová, M.; Ludacka, V.; Majková, E.; Siffalovic, P.; et al. Tuning the orientation of few-layer MoS$_2$ films using one-zone sulfurization. *RSC Adv.* **2019**, *9*, 29645–29651. [CrossRef]

51. Shahzad, R.; Kim, T.; Kang, S.W. Effects of temperature and pressure on sulfurization of molybdenum nano-sheets for MoS$_2$ synthesis. *Thin Solid Film.* **2017**, *641*, 79–86. [CrossRef]

52. Lee II, E.W.; Ma, L.; Nath, D.N.; Lee, C.H.; Arehart, A.; Wu, Y.; Rajan, S. Growth and electrical characterization of two-dimensional layered MoS$_2$/SiC heterojunctions. *Appl. Phys. Lett.* **2014**, *105*, 203504. [CrossRef]

53. Wang, H.; Zhang, Q.; Yao, H.; Liang, Z.; Lee, H.-W.; Hsu, P.-C.; Zheng, G.; Cui, Y. High electrochemical selectivity of edge versus terrace sites in two-dimensional layered MoS$_2$ materials. *Nano Lett.* **2014**, *14*, 7138–7144. [CrossRef] [PubMed]

54. Hadouda, H.; Pouzet, J.; Bernede, J.C.; Barreau, A. MoS$_2$ thin film synthesis by soft sulfurization of a molybdenum layer. *Mater. Chem. Phys.* **1995**, *42*, 291–297. [CrossRef]

55. Naujokaitis, A.; Gaigalas, P.; Bittencourt, C.; Mickevičius, S.; Jagminas, A. 1T/2H MoS$_2$/MoO$_3$ hybrid assembles with glycine as highly efficient and stable electrocatalyst for water splitting. *Int. J. Hydrog. Energy* **2019**, *44*, 24237–24245. [CrossRef]

56. Lloyd, D.; Liu, X.; Christopher, J.S.; Cantley, L.; Wadehra, A.; Kim, B.L.; Goldberg, B.B.; Swan, A.K.; Bunch, J.S. Band Gap Engineering with Ultralarge Biaxial Strains in Suspended Monolayer MoS$_2$. *Nano Lett.* **2016**, *16*, 5836–5841. [CrossRef] [PubMed]

57. Bampoulis, P.; van Bremen, R.; Yao, Q.; Poelsema, B.; Zandvliet, H.J.W.; Sotthewes, K. Defect Dominated Charge Transport and Fermi Level Pinning in MoS$_2$/Metal Contacts. *ACS Appl. Mater. Interfaces* **2017**, *9*, 19278–19286. [CrossRef]

58. Sotthewes, K.; van Bremen, R.; Dollekamp, E.; Boulogne, T.; Nowakowski, K.; Kas, D.; Zandvliet Harold, J.W.; Bampoulis, P. Universal Fermi-Level Pinning in Transition-Metal Dichalcogenides. *J. Phys. Chem. C* **2019**, *123*, 5411. [CrossRef] [PubMed]

59. Giannazzo, F.; Schilirò, E.; Greco, G.; Roccaforte, F. Conductive Atomic Force Microscopy of Semiconducting Transition Metal Dichalcogenides and Heterostructures. *Nanomaterials* **2020**, *10*, 803. [CrossRef] [PubMed]

60. Giannazzo, F.; Fisichella, G.; Piazza, A.; Agnello, S.; Roccaforte, F. Nanoscale Inhomogeneity of the Schottky Barrier and Resistivity in MoS$_2$ Multilayers. *Phys. Rev. B* **2015**, *92*, 081307. [CrossRef]

61. Zhu, H.; Qin, X.; Cheng, L.; Azcatl, A.; Kim, J.; Wallace, R.M. Remote Plasma Oxidation and Atomic Layer Etching of MoS$_2$. *ACS Appl. Mater. Interfaces* **2016**, *8*, 19119–19126. [CrossRef] [PubMed]

62. Giannazzo, F.; Fisichella, G.; Greco, G.; Di Franco, S.; Deretzis, I.; La Magna, A.; Bongiorno, C.; Nicotra, G.; Spinella, C.; Scopelliti, M.; et al. Ambipolar MoS$_2$ Transistors by Nanoscale Tailoring of Schottky Barrier Using Oxygen Plasma Functionalization. *ACS Appl. Mater. Interfaces* **2017**, *9*, 23164–23174. [CrossRef]

63. Hamada, T.; Tomiya, S.; Tatsumi, T.; Hamada, M.; Horiguchi, T.; Kakushima, K.; Tsutsui, K.; Wakabayashi, H. Sheet Resistance Reduction of MoS$_2$ Film Using Sputtering and Chlorine Plasma Treatment Followed by Sulfur Vapor Annealing. *IEEE J. Electron Devices Soc.* **2021**, *9*, 278–285. [CrossRef]

64. Giannazzo, F.; Bosi, M.; Fabbri, F.; Schilirò, E.; Greco, G.; Roccaforte, F. Direct Probing of Grain Boundary Resistance in Chemical Vapor Deposition-Grown Monolayer MoS$_2$ by Conductive Atomic Force Microscopy. *Phys. Status Solidi RRL* **2020**, *14*, 1900393. [CrossRef]

65. Golovynskyi, S.; Irfan, I.; Bosi, M.; Seravalli, L.; Datsenko, O.I.; Golovynska, I.; Li, B.; Lin, D.; Qu, J. Exciton and trion in few-layer MoS$_2$: Thickness- and temperature-dependent photoluminescence. *Appl. Surf. Sci.* **2020**, *515*, 146033. [CrossRef]

66. Mignuzzi, S.; Pollard, A.J.; Bonini, N.; Brennan, B.; Gilmore, I.S.; Pimenta, M.A.; Richards, D.; Roy, D. Effect of disorder on Raman scattering of single-layer MoS$_2$. *Phys. Rev. B* **2015**, *91*, 195411. [CrossRef]

67. Chow, P.K.; Jacobs-Gedrim, R.B.; Gao, J.; Lu, T.-M.; Yu, B.; Terrones, H.; Koratkar, N. Defect-Induced Photoluminescence in Monolayer Semiconducting Transition Metal Dichalcogenides. *ACS Nano* **2015**, *9*, 1520–1527. [CrossRef]

68. Watson, A.J.; Lu, W.; Guimaraes, M.H.D.; Stöhr, M. Transfer of large-scale two-dimensional semiconductors: Challenges and developments. *2D Mater.* **2021**, *8*, 032001. [CrossRef]